

On-chip directional octave-spanning supercontinuum generation from high order mode in near ultraviolet to infrared spectrum using AlN waveguides

Hong Chen¹, Jingan Zhou¹, Dongying Li¹, Dongyu Chen², Abhinav K. Vinod³, Houqiang Fu¹, Xuanqi Huang¹, Tsung-Han Yang¹, Jossue A. Montes¹, Kai Fu¹, Chen Yang¹, Cun-Zheng Ning^{1,4}, Chee Wei Wong³, Andrea M. Armani², and Yuji Zhao^{1,*}

¹School of Electrical, Computer and Energy Engineering, Arizona State University, Tempe, AZ 85287, USA

²Mork Family Department of Chemical Engineering and Materials Science, University of Southern California, Los Angeles, CA 90089, USA

³Department of Electrical Engineering, University of California, Los Angeles, CA 90095, USA

⁴Department of Electronic Engineering, Tsinghua University, Beijing 100084, China

*Correspondence to: yuji.zhao@asu.edu

Abstract: On-chip ultraviolet to infrared (UV–IR) spectrum frequency metrology is of crucial importance as a characterization tool for fundamental studies on quantum physics, chemistry, and biology. Due to the strong material dispersion, traditional techniques fail to demonstrate the device that can be applied to generate coherent broadband spectrum that covers the full UV–IR wavelengths. In this work, we explore several novel techniques for supercontinuum generation covering near-UV to near-IR spectrum using AlN micro-photonic waveguides, which is essential for frequency metrology applications: First, to create anomalous dispersion, high order mode (TE₁₀) was adopted, together with its carefully designed high efficiency excitation strategies. Second, the spectrum was broadened by soliton fission through third order dispersion and second harmonic generation, by which directional energy transfer from near-IR to near-UV can be obtained. Finally, high quality single crystalline AlN material was used to provide broadband transparency from UV to IR. Under decently low pulse energy of 0.36 nJ, the experimental spectrum from supercontinuum generation covers from 490 nm to over 1100 nm, with a second harmonic generation band covering from 405 nm to 425 nm. This work paves the way towards UV–IR full spectrum on-chip frequency metrology applications.

On-chip supercontinuum generation spanning from UV through IR with low (sub-nJ) powers has been a quest of researchers since the original demonstration in the 1960's [1,2]. An integrated system would enable research efforts and technology in white-light emitters [3,4], ultrahigh-resolution spectroscopy [5,6], high-speed interconnection [7], and quantum states generation [8,9]. While attempts have been made using a wide range of material systems [10-20] and nonlinear phenomena, this achievement has eluded the research community due to fundamental principles. Namely, the majority of attempts relied on a combination of self-phase modulation (SPM) and soliton fission (SF) processes where the solitons were perturbed by 4th order dispersion in fundamental transverse electric (TE) / transverse magnetic (TM) modes. Moreover, solitons perturbed by 4th order dispersion emits dispersive waves (DWs) in both blue and red shifting spectral, which degrades the energy efficiency for short wavelength applications. Despite the success in achieving broadband spectrum this strategy failed to reach below 500nm due to limits in material crystallinity and reliance on long wavelength pump sources. One exception is work based

on silica ridge waveguides which successfully reached into the UV range [13]. However, the low nonlinear coefficient of silica required large pump energies to be used. Therefore, to overcome this limit, a higher nonlinear material must be used. One such material is AlN. In a preliminary study, the high $\chi^{(2)}$ of AlN was used to achieve directional nonlinear energy transfer [18]. This approach enabled a spectrum covering over 100THz within the UV region using only 0.237nJ. Unfortunately, this system was limited to operation in the normal GVD range. In this work, these limitations are overcome to achieve supercontinuum generation from near-UV to near-IR with sub-nJ pulse energy.

To achieve supercontinuum generation covering near-UV to near-IR spectrum, several nonlinear optical processes can be proposed as the potential broadening mechanisms for the device design with both advantages and limitations. For example, SPM is the most commonly observed process in the initial stage of spectrum broadening, however it requires excessive high excitation power to further expand the spectrum [21]; Four-wave mixing is applied in numerous studies [22] of micro-comb systems, however it generally requires fine resonating device structures; Harmonic generation provides good directional energy transfer, however it has limited bandwidth due to the phase-matching conditions [18]; Self-steepening has the potential for broadband directional supercontinuum generation in UV–visible range, however it requires small and flat dispersion near pumping wavelengths to build the steep temporal structures [15], which is hindered by the strong material dispersion in the near-visible spectrum; Other nonlinear processes such as Stokes scattering [23] and modulation instability [23] are usually accompanied with strong phase noise thus are not favorable. To tackle the issues mentioned above, several advances in engineering and in science are simultaneously combined in an AlN integrated waveguide [Figure 1(a)]. First, to create anomalous dispersion, a high order waveguide mode (TE_{10}) was used. To efficiently excite this mode, a high efficiency excitation strategy was designed and fabricated. Second, the spectrum was broadened by soliton fission through third order dispersion and second harmonic generation. This approach allowed directional energy transfer from near-IR to near-UV to be obtained. Third, high quality single crystalline AlN material was used to provide broadband transparency from UV to IR. The development and use of high quality single crystalline of AlN improved the optical performance of the device, allowing the nonlinear processes to occur simultaneously and with high efficiency. As a result of these advances, supercontinuum generation from 490 nm to over 1100 nm, with a second harmonic generation band covering from 405 nm to 425 nm is achieved with only 0.36nJ of pulse energy. This work paves the way towards UV–IR full spectrum on-chip frequency metrology applications.

Results

To optimize the dispersion of the AlN waveguide, the modal dispersion for a series of waveguide geometries was computed from an in-house made numerical solver based on finite-difference method (FDM) provided in [24]. The computed dispersions were compared with commercial software (Lumerical modes) to confirm accuracy. These calculations were used to direct the device design and mode selection. For example, the calculated GVDs in a $1.1 \mu\text{m} \times 1.2 \mu\text{m}$ ($W \times H$) waveguide is shown in Fig. 1(b). Due to the highly dispersive material property, TE_{00} and TM_{00} modes exhibit normal dispersion below 1000 nm, while TE_{10} mode shows anomalous dispersion

above 740 nm. Anomalous dispersion supports the formation of solitons near the operating wavelengths of Ti:sapphire laser. The zero dispersion wavelength (ZDW) of this TE_{10} mode is widely tunable by varying waveguide widths, as illustrated in Fig. 1(c).

Using these calculations as the basis for device fabrication design, single crystalline AlN thin films were epitaxially grown by metalorganic chemical vapor deposition (MOCVD) on sapphire substrates. The surface roughness was determined by atomic force microscopy (AFM) in a $5 \mu\text{m} \times 5 \mu\text{m}$ scan with a root mean squared (RMS) roughness of ~ 3 nm. Refractive indexes of the thin films were measured by ellipsometry. Figure 1(d) shows the schematic view of the device structure of the AlN waveguide, where the waveguide geometrical parameters, such as width (W), height (H), and sidewall angles (θ), are defined. Waveguides were fabricated from 1.2 μm thick films (H) with widths ranging from 0.8 μm to 1.6 μm and lengths around 0.6 cm. Figure 1(e) shows the representative cross-section transmission electron microscopy (TEM) image of the AlN waveguide. The crystalline nature of the AlN thin film is clearly evident. Additional material data and waveguide fabrication details are in the Methods section.

The experimental setup is depicted in Fig. 1(f). A standard Ti:sapphire laser (Spectra Physics) with 100 fs pulse width (full-width half maximum) and 82 MHz repetition rate was used. To couple light into the on-chip waveguides from the free-space laser, end-fire coupling was used. The out scattered light from the waveguides was collected by a linear CMOS camera (Thorlabs DCC1240) and used to perform propagation loss estimation. A tapered fiber was placed near the output port of waveguides and the output signal was fed into optical spectrum analyzer (Yokogawa AQ6373B). Coupling strategies to efficiently excite the high order modes are discussed in the Methods section.

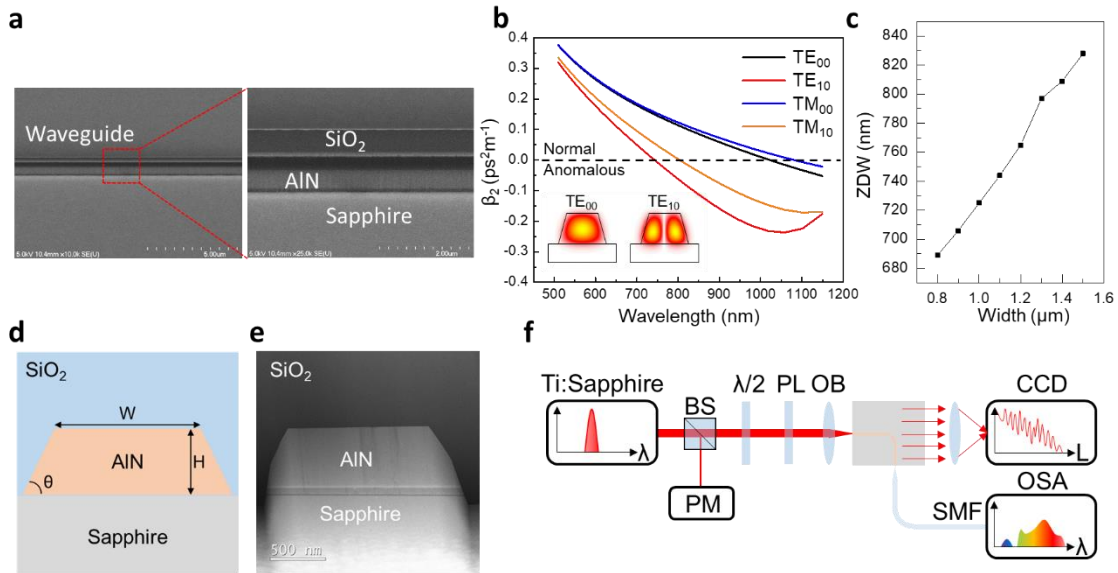


Figure 1. (a) Scanning electron microscope image of AlN waveguides fabricated in this research. The SiO₂ hardmask is remaining on the top. Smooth sidewall can be identified from the zoomed image. (b) Calculated group velocity dispersions of TE₀₀, TE₁₀, TM₀₀, and TM₁₀ modes in a 1.1 $\mu\text{m} \times 1.2 \mu\text{m}$ ($W \times H$) AlN waveguide, the insertion shows the mode profiles ($|E_x|$) of TE₀₀ and TE₁₀ modes, which are the modes that utilized within this work. (c) Zero-dispersion

wavelength vs. waveguide geometry, the height was kept at 1.2 μm . (d) Schematic view of the device structure of the AlN waveguide, where the waveguide geometries such as width (W), height (H), and sidewall angles (θ) are defined. (e) Transmission electron microscope image of a typical AlN waveguide fabricated in this work. (f) Experimental setup implemented in this work.

A broadband supercontinuum spectrum is shown in Fig. 2(a). The main spectrum spans from 490 nm to 1100 nm, which is over one octave. Due to the large second order susceptibility of AlN, a secondary spectrum was observed from 405 nm to 425 nm. The pumping wavelength was slightly tuned near 800 nm, and the best spectrum [Figure 2(a)] was recorded at $\lambda = 810$ nm. Minor changes were observed when varying the pumping wavelength from 800 nm to 820 nm.

The broadened spectrum can be identified as the composition of TE_{00} and TE_{10} modes. Due to the ultra-short pulse width and different group velocities, the TE_{00} and TE_{10} modes split in the temporal domain after a propagation length of a few microns. Therefore, throughout this study, the mutual nonlinear coupling between TE_{00} and TE_{10} modes were neglected. By comparing the propagation loss and on-chip average power of $\text{TE}_{00}/\text{TE}_{10}$ modes, the power difference between TE_{00} and TE_{10} mode can be justified to be ~ 10 dB. According to the numerical simulation, the excitation efficiencies of TE_{00} and TE_{10} modes are 15% and 20%, respectively (see S.I.). On-chip average power was estimated to be ~ 50 mW, thus the average power within TE_{10} mode was estimated to be 30 mW, corresponding to a pulse energy of 0.36 nJ, which is low when compared with other supercontinuum generation methods at short wavelengths [13,15,17].

By solving the nonlinear Schrodinger's equation (NSE), the simulated spectrum for each mode can be obtained which is also shown in the spectrum plot in Fig. 2(a). Details in regard to NSE simulation can be found in "method". As predicted in Figure 1(c), the TE_{00} mode was propagating within normal dispersion region, therefore self-phase modulation is the major contributor to its broadening mechanism. In contrast, for the TE_{10} mode, the pulse was split into its continent fundamental solitons, and the solitons were perturbed by TOD. Therefore, DWs were emitted near 500 nm through non-solitonic radiation, enabling the formation of the broadband supercontinuum in the TE_{10} mode case.

Under high power excitations, complex physical processes are expected such as strong thermal effects [25], multi-photon absorption [26], free carrier dispersion [26], cross-phase modulation [27], modulation instability [28], and mode avoid-crossing [29]. Under such conditions, the NSE only provides good estimation on spectrum width, but cannot accurately predicts the spectrum shape at all wavelengths. Therefore, to further confirm the non-solitonic radiation process, a series of low excitation power measurements were performed, and the corresponding spectra were recorded (Figs. 2(b)-2(d)). When the average pumping power is below 10 mW, the self-phase modulation process is responsible for the symmetric broadening as indicated in Figs. 2(b) and 2(c). When the average pumping power reaches 10 mW which corresponds to a pulse energy of only 0.12 nJ, significant asymmetric broadening starts to initiate as shown in Fig. 2(d). The development of supercontinuum spectrum with increasing power can be further illustrated using Fig. 2(e). The spectral broadening was first initiated symmetrically by SPM (point 1 to 2), and then asymmetrically expanded by DW emission (point 2 to 3). From point 3 to 4, blue shifts of DW can

be observed, which is a result from the power dependent phase matching condition for DWs [23]:

$$\beta(\omega) = \beta(\omega_s) + \beta_1(\omega - \omega_s) + \frac{1}{2}\gamma P_s \quad (1)$$

where β indicates wavevector. ω_s and ω indicate angular frequency of soliton and DW, respectively. β_1 is equal to $\partial\beta/\partial\omega$. P is the power within soliton modes. γ is the nonlinear parameter that described by $(\omega n_2)/(cA_{\text{eff}})$, where the c and A_{eff} indicate vacuum speed of light and effective modal area, respectively. The blue shifts of DW with increasing power can be attributed to the power dependent term in the Eq. (1).

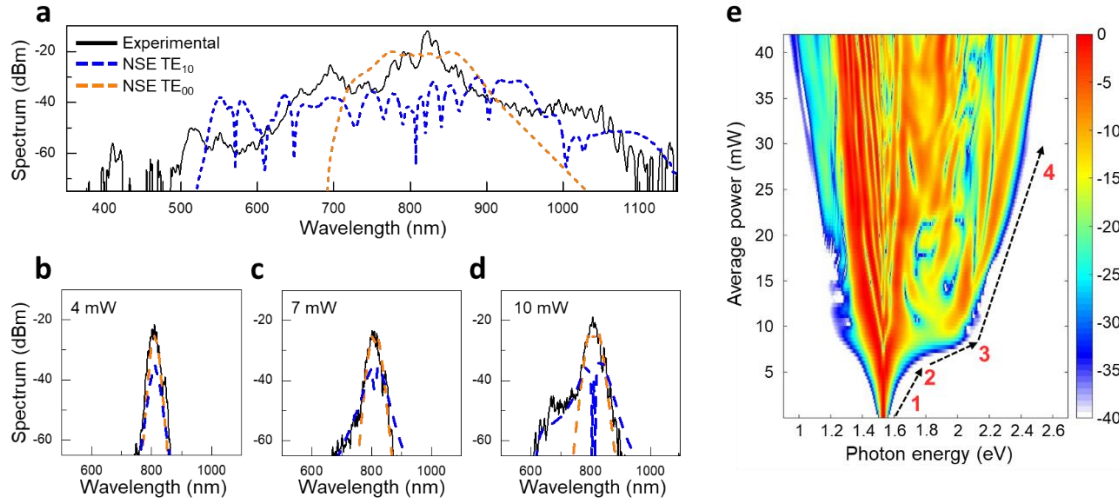


Figure 2. (a) Experimental results of the supercontinuum spectrum (black solid), and the nonlinear Schrodinger's equation (NSE) simulated spectrum of TE₀₀ (orange dash) and TE₁₀ (Blue dash) modes for the AlN waveguide. The spectrum is generated with a pump wavelength of 810nm and at average pump power of 30 mW. (b)-(d) The experimental (black solid) and the NSF simulated results (orange and blue dash) under low power pumping conditions. (e) Spectral evolutions of the AlN waveguide at different average pumping powers (within TE₁₀ mode) used in the measurements. From point 1–2, 2–3, and 3–4, the broadening mechanism was governed by SPM, SF, and optical power dependent phase-matching between soliton and DW.

Given the dependence shown in Figure 2e, it is apparent that, unlike the prior results on supercontinuum generation that relies on the 4th order dispersion, the spectrum obtained in this work exhibits strong dependence on waveguide geometry due to the near ZDW pumping. To further investigate this dependence and create a generalizable waveguide design strategy, the GVD, TOD, and 4th order dispersion curves for AlN waveguides with different widths are calculated (Figure 3(a)). A waveguide width below 1200 nm is required to support the solitons near pumping wavelengths. It is also noteworthy that below a waveguide width of 800 nm, perturbation on solitons are mainly due to the 4th order dispersion from the sudden decrease of β_3 , which results in DWs emission towards unwanted spectral wavelengths. Moreover, as is estimated in Fig. 3(b), the propagation loss of the TE₁₀ mode increases exponentially with reducing waveguide widths, which exceeds 50 dB/cm at a waveguide width of 1000 nm. This strong loss prohibits the formation of fundamental solitons [26], which in turn prevents the DW emission.

Combining the observations in Figs. 3(a) and 3(b), the design space of the AlN waveguide devices for this work is limited within a waveguide width from ~ 1000 nm to ~ 1200 nm. To verify these calculations, devices outside of this optimum range are fabricated and characterized. Figure 3(c) illustrates the measured spectrum and the NSE simulated pulse spectrum for the TE₀₀ mode in AlN waveguides with widths of 800 nm and 1400 nm. The broadening processes in these two waveguide designs can be clearly identified as SPM, and the average pumping power within the TE₁₀ was estimated to be ~ 20 mW, which is two times higher than that in case of Fig. 2(d).

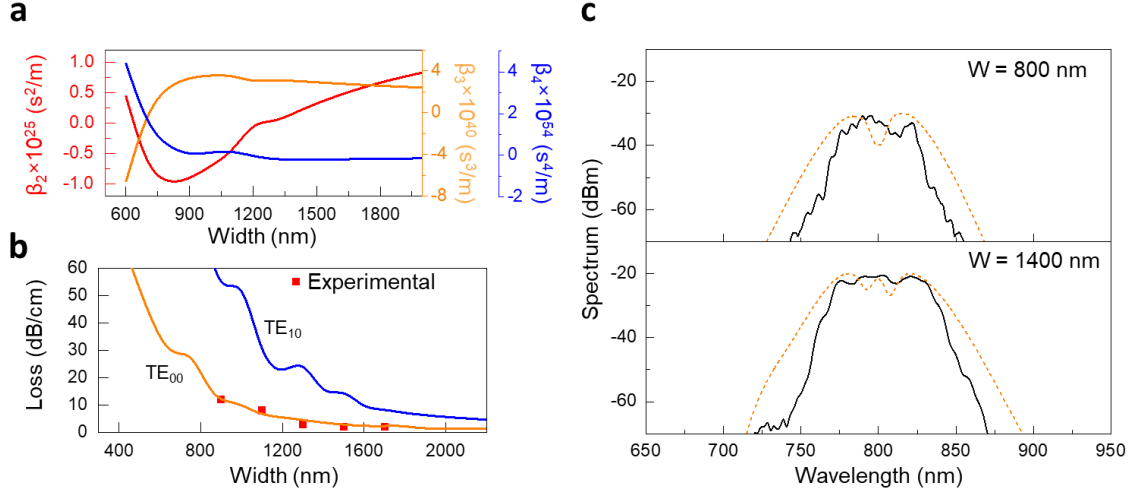


Figure 3. (a) The calculated GVD (β_2), TOD (β_3), and 4th order dispersion (β_4) curves for AlN waveguides with different widths, represented by red, orange, and blue curves, respectively. (b) Experimentally measured propagation loss (square points) in dB/cm and the calculated propagation loss for TE₀₀ (orange curve), TE₁₀ (blue curve) modes for AlN waveguides with different widths. (c) Measured spectrum (black curve) and the NSE simulated pulse spectrum (orange dash curve) for TE₀₀ mode in AlN waveguides with widths of 800 nm and 1400 nm. The spectrum was mainly broadened by SPM of the fundamental TE₀₀ mode, therefore the simulated spectral for the TE₁₀ mode are not shown here.

While the generation of the primary spectrum from 490 nm to 1100 nm with only 0.36nJ is remarkable, the simultaneous generation of an even higher energy (lower wavelength) secondary spectrum spanning from 405 to 425 nm further increasing the potential impact of this system. To understand the physical mechanism that gives rise to this secondary spectrum, we solve for the mode dispersion near the fundamental and the SHG wavelengths, and the mode profiles of high order modes near SHG wavelengths are depicted in Fig. 4(a). Figure 4(b) shows the modal dispersion of TE₀₀ mode and TE₁₀ mode near 800 nm, and the dispersion of several high order modes near 400 nm. By optimizing the waveguide coupling design, modal phase-matching was achieved at 398 nm and 412 nm. Furthermore, Fig. 4(b) also shows the dispersion curve of TE₁₀ mode in the near-visible region. Since the phase-matching point is far away from 400 nm, and the two phase-matching points have wavelength difference of over 40 nm, we neglect the SHG effect from the TE₁₀ mode. The experimental identified second harmonic signal was recorded at 407 nm and 421 nm and is shown in Fig. 4(c). The MOCVD growth and the dry etching processes for the AlN waveguides may cause minor geometry discrepancy between the simulation and the

experiment, which resulted in the small differences between the simulated and experimentally recorded phase matching points. Since the phase-matching wavelengths are dependent on the device geometry, the location of SHG signal is invariant to pumping wavelengths, which is evident in Fig. 4(c).

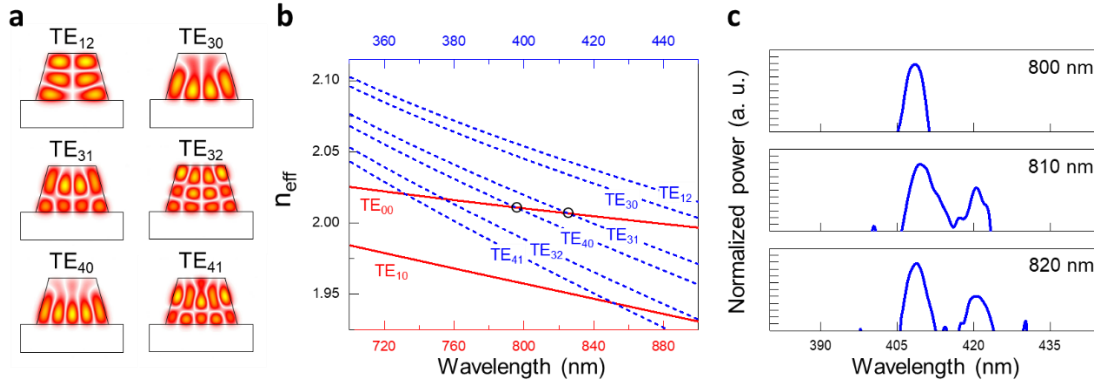


Figure 4. (a) Mode profile ($|E_x|$) of each high order mode computed at 400 nm wavelength. (b) The modal dispersion of TE₀₀ mode and TE₁₀ mode near 800 nm (red curves) and the dispersion of several high order modes near 400 nm (blue dash curves) for the secondary spectrum from 405 to 425 nm in Fig. 2(a). Phase matching wavelengths can be determined at the crossing points of the curves. The two peaks measured from experiment can be identified at the two circle-marked points. (c) SHG signal near 400 nm at different pumping wavelengths, the locations of the SHG peaks were invariant to pumping wavelengths.

The optical coherence of the spectrum can be determined by applying the first-order coherence function [10,14,17]:

$$|g_{12}^{(1)}(\lambda)| = \left| \frac{\langle E_1^*(\lambda)E_2(\lambda) \rangle}{\sqrt{\langle |E_1(\lambda)|^2 \rangle \langle |E_2(\lambda)|^2 \rangle}} \right| \quad (2)$$

which is the ensemble average of multiple supercontinuum pulses. The simulation took 100 supercontinuum pulses with a standard shot noise at the input spectra, and the obtained first-order coherence of TE₁₀ supercontinuum is shown in Fig. 5. The coherence is close to unity from visible to near-infrared, which indicates the broadening strategy applied in this work is robust to noise.

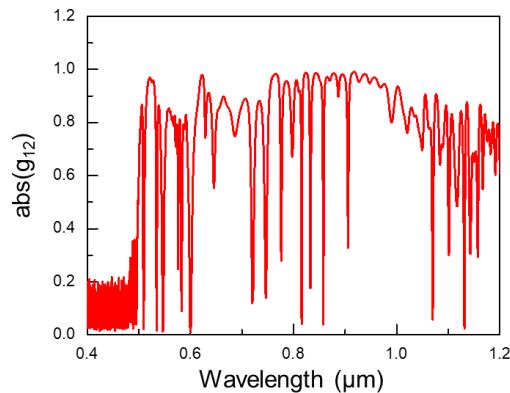


Figure 5. The simulated first-order coherence function vs. wavelengths for AlN waveguide with a width of 1.2 μm . The coherent function is near unity across the whole spectrum, indicating that the broadening mechanism is robust to shot noise.

Conclusion

In conclusion, we obtained supercontinuum generation from dispersion engineered AlN waveguide, the optical energy of which directionally transferred from near-IR towards near-UV wavelengths. The main spectrum covers from 490 nm to over 1100 nm with a secondary SHG spectrum that covers from 405 nm to 425 nm. Near-visible pumping was implemented to improve energy efficiency. To overcome the strong material dispersion, the AlN waveguides were designed to support high order modes. The experiment results were compared with the theoretical results from NSE simulation, which confirmed that DWs were generated from solitons perturbed by TOD, allowing for directional energy transfer. Further investigations on high order dispersion terms and propagation losses reveal that the SF process can only be initiated within a narrow window of waveguide width, which was supported by experimental observations. The SHG spectrum was investigated by solving modal dispersions near 800 nm and 400 nm, and the corresponding phase-matching wavelengths were determined. Simulation on first-order coherence function suggests that the spectrum broadening procedure is robust to noise, which is essential for frequency metrology related applications. This work provides novel waveguide design strategies and paves the way towards UV–IR frequency comb generations.

Methods:

Fabrication AlN waveguides. The AlN thin films were coated with a ~ 600 nm SiO_2 layer using plasma enhanced chemical vapor deposition (PECVD), followed by an 80 nm Cr layer using electron-beam evaporation. The two layers served as hardmasks for the dry etching processes. Photoresist ma-N 2403 was used to perform electron-beam lithography (EBL). The Cr layer was etched away using a user developed (chlorine + argon) reactive ion etching (RIE) process, while the SiO_2 layer was removed by standard anisotropic RIE etching process developed by ASU NanoFab. The AlN waveguide patterns were defined using a user developed inductively coupled plasma (ICP) etching with Cl_2 , BrCl_3 , and Ar chemistries at a bias voltage near 300V. The waveguides were coated by 2 μm SiO_2 coating layers to reduce scattering loss. After fabrication processes, samples were cut and polished down to 0.1 μm grade. The fabricated waveguide has ~ 50 to 100 nm width variance due to the underneath isotropic etching during Cr etching process, this variance was involved in numerical simulations. Detailed process flow and scanning electron microscope (SEM) images of the fabricated AlN waveguides can be found in S.I.

Simulation on pulse propagation. The pulse propagation along the waveguide was simulated using an in-house developed solver for nonlinear Schrodinger's equation using split-step Fourier method [23], where the 4th order Runge-Kutta method [30] was also implemented to reduce

computation load. The format of the nonlinear Schrodinger's equation was:

$$\frac{\partial A}{\partial z} = -\frac{\alpha}{2}A + i \sum_{k \geq 2} i^k \frac{\beta_k}{k!} \frac{\partial^k A}{\partial t^k} + i\gamma[|A|^2A + \frac{i}{\omega_0} \frac{\partial}{\partial t} (|A|^2A) - T_R A \frac{\partial |A|^2}{\partial t}] \quad (3)$$

where $A(z,t)$ denotes the pulse slow varying amplitude, α is the propagation loss, β_k is the k th order dispersion, γ is the nonlinear parameter, and T_R is the Raman response parameter. It should be noted that we keep the most simplified Raman response form in Eq. (3), and the T_R was set to zero as no significant red-shifted spectrum was observed through this whole study. Dispersion terms were truncated at 6th order, but it's noteworthy that only TOD plays significant role in modifying the spectrum. The Kerr refractive index of AlN was estimated to be $2.5 \times 10^{-19} \text{ m}^2/\text{W}$, which gives a nonlinear parameter $\gamma \sim 3 \text{ W}^{-1}\text{m}^{-1}$ depending on the mode effective area. The initial pulse shape was assumed to be Gaussian type with a full-width-at-half-maximum (FWHM) of 100 fs.

High order mode excitations. We adopted different waveguide excitation strategies in this work, the detailed descriptions (Pros. and Cons.) of each excitation methods are discussed in S.I.. The most efficient excitation method was applying normal taper with a $\sim 5 \mu\text{m}$ taper width. Under low power operation, the beam was first focused at the center of taper, then slowly varying the nano-stage to move the focal point from center to the edge of taper facet. The out-scattered light was monitored by CMOS camera at the same time. Since the TE_{10} mode has higher scattering loss comparing to the TE_{00} mode, when the out-scattered light reaches its maximum (as recorded by CMOS camera), the excitation efficiency of TE_{10} mode will be near its maximum. At this stage, the location of focusing point is near the edge of taper facet, which can be confirmed by the CMOS camera. An alternative way to excite TE_{10} mode was to operate the system under higher power (near 30 mW on-chip average pumping power). By slowly varying the focal point from center to the edge of taper, DWs near 600 nm were generated due to the increasing excitation efficiency of the TE_{10} mode. The red radiation can be directly observed under microscope, and the excitation efficiency of the TE_{10} mode can be optimized by maximizing the red radiation.

Estimation of propagation loss. The propagation losses of TE_{00} modes were experimentally characterized by collecting out-scattered light along the propagation direction using a CMOS camera similar to our previous investigation in [31]. The typical scattered optical power versus propagation length is provided in S.I.. By adopting semi-log plotting, the decay slope is proportional to propagation loss of TE_{00} mode in dB/cm. The low loss of TE_{00} mode was further confirmed by measuring its intrinsic quality factor of ring resonators (See S.I.).

The losses of TE_{00} modes with different waveguide widths were fitted by an in-house made dyadic Green's function (DGF) solver to obtain the sidewall roughness. The detailed description on DGF can be found in S.I.. DGF fitting gives sidewall roughness around 4 nm, which agrees well with standard optimized ICP etching process. By plugging in TE_{10} mode profile and sidewall roughness, the scattering loss can be estimated.

Supplementary information

The supplementary information includes material characterization, fabrication process flow, waveguide performance evaluation, high order mode excitation efficiency, propagation loss estimation, and auxiliary experimental data.

Acknowledgments

This work was supported by the grant from Army Research Office monitored by Dr. Michael Gerhold. We gratefully acknowledge the use of facilities within the LeRoy Eyring Center for Solid State Science, ASU NanoFab, and ASU CLAS ultra-fast laser facility. We received great supports from ASU nanophotonics group lead by Prof. Cun-Zheng Ning. The authors would also like to thank Dr. Su Lin and Dr. Douglas Daniel for their great assistance in the early state of this research.

Author contributions

Y.Z. initiated this research and supervised the project progress. H.C. coded the numerical solvers, designed the waveguides, fabricated the devices, and performed the optical testing. J.Z. and D.L. (supervised by C.Z.N.) participated in the optical testing of the late devices within the laboratory. D.C. (supervised by A.M.A.) and A.K.V. (supervised by C.W.W) evaluated waveguide performance of GaN and AlN by measuring the Q factor of the resonators and provided valuable discussions. H.C., J.Z., H.F., X.H., T.H.Y., and J.A.M. carried out the material characterizations (ellipsometry, XRD, AFM, SEM, etc.). K.F. and C.Y. assisted the device fabrication. H.C. and Y.Z. wrote the manuscript with inputs and suggestions from other authors. All authors participated in data analysis and discussions, and contributed significantly to this work.

References:

1. Jones, W.J. and Stoicheff, B.P., 1964. Inverse Raman spectra: induced absorption at optical frequencies. *Physical Review Letters*, 13(22), p.657.
2. Stoicheff, B.P., 1963. Characteristics of stimulated Raman radiation generated by coherent light. *Physics Letters*, 7(3), pp.186-188.
3. Fan, F., Turkdogan, S., Liu, Z., Shelhammer, D. and Ning, C.Z., 2015. A monolithic white laser. *Nature nanotechnology*, 10(9), p.796.
4. Rosemann, N.W., Eußner, J.P., Beyer, A., Koch, S.W., Volz, K., Dehnen, S. and Chatterjee, S., 2016. A highly efficient directional molecular white-light emitter driven by a continuous-wave laser diode. *Science*, 352(6291), pp.1301-1304.
5. Suh, M.G., Yi, X., Lai, Y.H., Leifer, S., Grudinin, I.S., Vasisht, G., Martin, E.C., Fitzgerald, M.P., Doppmann, G., Wang, J. and Mawet, D., 2019. Searching for Exoplanets Using a Microresonator Astrocomb. *Nature photonics*, 13, pp.25-30.
6. Rosenband, T., Hume, D.B., Schmidt, P.O., Chou, C.W., Brusch, A., Lorini, L., Oskay, W.H., Drullinger, R.E., Fortier, T.M., Stalnaker, J.E. and Diddams, S.A., 2008. Frequency ratio of Al⁺ and Hg⁺ single-ion optical clocks; metrology at the 17th decimal place. *Science*, 319(5871), pp.1808-1812.
7. Pfeifle, J., Brasch, V., Lauermann, M., Yu, Y., Wegner, D., Herr, T., Hartinger, K., Schindler, P., Li, J., Hillerkuss, D. and Schmogrow, R., 2014. Coherent terabit communications with microresonator Kerr frequency combs. *Nature photonics*, 8(5), p.375.
8. Reimer, C., Kues, M., Roztocky, P., Wetzl, B., Grazioso, F., Little, B.E., Chu, S.T., Johnston, T., Bromberg, Y., Caspani, L. and Moss, D.J., 2016. Generation of multiphoton entangled quantum states by means of integrated frequency combs. *Science*, 351(6278), pp.1176-1180.
9. Chen, M., Menicucci, N.C. and Pfister, O., 2014. Experimental realization of multipartite entanglement of 60 modes of a quantum optical frequency comb. *Physical review letters*, 112(12), p.120505.
10. Kuyken, B., Ideguchi, T., Holzner, S., Yan, M., Hänsch, T.W., Van Campenhout, J., Verheyen, P., Coen, S., Leo, F., Baets, R. and Roelkens, G., 2015. An octave-spanning mid-infrared frequency comb generated in a silicon nanophotonic wire waveguide. *Nature communications*, 6, p.6310.
11. Singh, N., Xin, M., Vermeulen, D., Shtyrkova, K., Li, N., Callahan, P.T., Magden, E.S., Ruocco, A., Fahrenkopf, N., Baiocco, C. and Kuo, B.P., 2018. Octave-spanning coherent supercontinuum generation in silicon on insulator from 1.06 μm to beyond 2.4 μm . *Light: Science & Applications*, 7(1), p.17131.
12. Dave, U.D., Ciret, C., Gorza, S.P., Combrie, S., De Rossi, A., Raineri, F., Roelkens, G. and Kuyken, B., 2015. Dispersive-wave-based octave-spanning supercontinuum generation in InGaP membrane waveguides on a silicon substrate. *Optics letters*, 40(15), pp.3584-3587.
13. Oh, D.Y., Yang, K.Y., Fredrick, C., Ycas, G., Diddams, S.A. and Vahala, K.J., 2017. Coherent ultra-violet to near-infrared generation in silica ridge waveguides. *Nature communications*, 8, p.13922.
14. Guo, H., Herkommer, C., Billat, A., Grassani, D., Zhang, C., Pfeiffer, M.H., Weng, W., Brès, C.S. and Kippenberg, T.J., 2018. Mid-infrared frequency comb via coherent dispersive wave generation in silicon nitride nanophotonic waveguides. *Nature Photonics*, 12(6), p.330.
15. Zhang, L., Yan, Y., Yue, Y., Lin, Q., Painter, O., Beausoleil, R.G. and Willner, A.E., 2011. On-chip two-octave supercontinuum generation by enhancing self-steepening of optical pulses. *Optics express*, 19(12), pp.11584-11590.

16. Chen, B.Q., Zhang, C., Hu, C.Y., Liu, R.J. and Li, Z.Y., 2015. High-efficiency broadband high-harmonic generation from a single quasi-phase-matching nonlinear crystal. *Physical review letters*, 115(8), p.083902.
17. Hickstein, D.D., Jung, H., Carlson, D.R., Lind, A., Coddington, I., Srinivasan, K., Ycas, G.G., Cole, D.C., Kowligy, A., Fredrick, C. and Droste, S., 2017. Ultrabroadband supercontinuum generation and frequency-comb stabilization using on-chip waveguides with both cubic and quadratic nonlinearities. *Physical Review Applied*, 8(1), p.014025.
18. Liu, X., Bruch, A.W., Lu, J., Gong, Z., Surya, J.B., Zhang, L., Wang, J., Yan, J. and Tang, H.X., 2019. Beyond 100 THz-spanning ultraviolet frequency combs in a non-centrosymmetric crystalline waveguide. *arXiv preprint arXiv:1906.00323*.
19. Stark, S.P., Travers, J.C. and Russell, P.S.J., 2012. Extreme supercontinuum generation to the deep UV. *Optics letters*, 37(5), pp.770-772.
20. Jiang, X., Joly, N.Y., Finger, M.A., Babic, F., Wong, G.K., Travers, J.C. and Russell, P.S.J., 2015. Deep-ultraviolet to mid-infrared supercontinuum generated in solid-core ZBLAN photonic crystal fibre. *Nature Photonics*, 9(2), p.133.
21. Boyraz, O., Indukuri, T. and Jalali, B., 2004. Self-phase-modulation induced spectral broadening in silicon waveguides. *Optics Express*, 12(5), pp.829-834.
22. Del'Haye, P., Schliesser, A., Arcizet, O., Wilken, T., Holzwarth, R. and Kippenberg, T.J., 2007. Optical frequency comb generation from a monolithic microresonator. *Nature*, 450(7173), p.1214.
23. Agrawal, G.P., 2000. Nonlinear fiber optics. In *Nonlinear Science at the Dawn of the 21st Century* (pp. 195-211). Springer, Berlin, Heidelberg.
24. Fallahkhair, A.B., Li, K.S. and Murphy, T.E., 2008. Vector finite difference modesolver for anisotropic dielectric waveguides. *Journal of Lightwave Technology*, 26(11), pp.1423-1431.
25. Martin-Lopez, S., Gonzalez-Herraez, M., Corredera, P., Hernanz, M.L., Carrasco, A. and Mendez, J.A., 2006. Temperature effects on supercontinuum generation using a continuous-wave Raman fiber laser. *Optics communications*, 267(1), pp.193-196.
26. Ciret, C., Gorza, S.P., Husko, C., Roelkens, G., Kuyken, B. and Leo, F., 2018. Physical origin of higher-order soliton fission in nanophotonic semiconductor waveguides. *Scientific reports*, 8(1), p.17177.
27. Genty, G., Lehtonen, M. and Ludvigsen, H., 2004. Effect of cross-phase modulation on supercontinuum generated in microstructured fibers with sub-30 fs pulses. *Optics express*, 12(19), pp.4614-4624.
28. Dudley, J.M., Genty, G., Dias, F., Kibler, B. and Akhmediev, N., 2009. Modulation instability, Akhmediev Breathers and continuous wave supercontinuum generation. *Optics express*, 17(24), pp.21497-21508.
29. Yang, Q.F., Yi, X., Yang, K.Y. and Vahala, K., 2016. Spatial-mode-interaction-induced dispersive waves and their active tuning in microresonators. *Optica*, 3(10), pp.1132-1135.
30. Hult, J., 2007. A fourth-order Runge–Kutta in the interaction picture method for simulating supercontinuum generation in optical fibers. *Journal of Lightwave Technology*, 25(12), pp.3770-3775.
31. Chen, H., Fu, H., Huang, X., Zhang, X., Yang, T.H., Montes, J.A., Baranowski, I. and Zhao, Y., 2017. Low loss GaN waveguides at the visible spectral wavelengths for integrated photonics applications. *Optics express*, 25(25), pp.31758-31773.